



Temporal analysis of land cover change in Ayapel's alluvial gold mining zones, Colombia

Maura Melissa Herrera¹, David Stephen Fernández², Fabio de Jesús Vélez³, Néstor Jaime Aguirre⁴
maura.herrera@udea.edu.co¹, david.fernandez@udea.edu.co², fabio.velez@udea.edu.co³, nestor.aguirre@udea.edu.co⁴
Universidad de Antioquia, Medellín, Colombia

ABSTRACT

Alluvial gold mining has been a longstanding economic activity in the municipality of Ayapel, Córdoba, dating back to the colonial era, as noted by historians. However, most of this mining has occurred outside legal frameworks, often facilitated by the presence of lawless groups. This illegality complicates efforts to monitor and implement ecological restoration plans in the area. Additionally, the municipality of Ayapel is home to a significant natural asset: La Ciénaga de Ayapel. Designated as a RAMSAR site since 2018, this wetland holds international recognition for its ecological importance. However, it faces the threat of contamination from the nearby mining activities. Therefore, monitoring this mining activity becomes a crucial point to ensure, among other components, the care of La Ciénaga de Ayapel. The objective of this study is to analyze land cover changes in areas affected by alluvial mining between 1985 and 2020, using Landsat images, digital image processing techniques, unsupervised classification, and sequential pattern mining for the multitemporal analysis.

Regarding the analysis conducted for the study area, encompassing the Quebradona microbasin in the municipality of Ayapel, for the years 1985 to 2020, there was an increase in mining activity of 503 ha, equivalent to 12 times that of 1985, with a peak in 2010, 54 times the 1985 levels. Bare soil, on the other hand, increased by 96% by 2020. As for vegetation cover, dense or high vegetation remained relatively constant over time, going from 2434 ha in 1985 to 2446 ha in 2020. Low vegetation, typically corresponding to grasslands, increased from occupying 3855 ha in 1985 to 5859 ha by 2020. Medium vegetation decreased by 25% compared to 1985, going from 7588 ha to 5674 ha by 2020. Finally, compared to 2010, there was a 14% increase or recovery in medium vegetation, and high vegetation saw a 5% recovery. It is important to highlight that the images from 1989 and 2013 exhibited a significant presence of cloud cover, which led to an underestimation of the area classified for each type of land cover.

Keywords: Remote Sensing, alluvial gold mining, satellite imagery, Landsat, land cover change, sequential pattern mining.

Análisis temporal del cambio de coberturas terrestres en zonas de minería de oro de aluvión en Ayapel, Colombia

RESUMEN

La minería de oro de aluvión ha sido una actividad económica de larga data en el municipio de Ayapel, Córdoba, con antecedentes que se remontan a la época colonial, según lo señalan los historiadores. Sin embargo, la mayor parte de esta minería ha ocurrido fuera de los marcos legales, a menudo facilitada por la presencia de grupos al margen de la ley. Esta ilegalidad dificulta los esfuerzos de monitoreo y la implementación de planes de restauración ecológica en la zona. Además, el municipio de Ayapel alberga un importante recurso natural: La Ciénaga de Ayapel. Este humedal ha sido designado como sitio RAMSAR desde 2018, lo que le otorga reconocimiento internacional por su importancia ecológica. No obstante, enfrenta la amenaza de contaminación debido a las actividades mineras cercanas. Por lo tanto, el monitoreo de esta actividad minera se vuelve un aspecto crucial para garantizar, entre otros elementos, la protección de La Ciénaga de Ayapel. El objetivo de este estudio es analizar los cambios en la cobertura terrestre en las áreas afectadas por la minería aluvial entre 1985 y 2020, utilizando imágenes Landsat, técnicas de procesamiento digital de imágenes, clasificación no supervisada y minería de patrones secuenciales para el análisis multitemporal.

En cuanto al análisis realizado en la zona de estudio, que abarca la microcuenca Quebradona en el municipio de Ayapel, se observó un incremento en la actividad minera de 503 ha entre los años 1985 y 2020, lo que equivale a 12 veces la extensión de 1985, alcanzando un pico en 2010, cuando la actividad minera fue 54 veces mayor que en 1985. Por otro lado, el suelo desnudo aumentó en un 96% para 2020. En cuanto a la cobertura vegetal, la vegetación densa o alta se mantuvo relativamente constante a lo largo del tiempo, pasando de 2434 ha en 1985 a 2446 ha en 2020. La vegetación baja, que generalmente corresponde a pastizales, creció de 3855 ha en 1985 a 5859 ha en 2020. En contraste, la vegetación media disminuyó en un 25% respecto a 1985, pasando de 7588 ha a 5674 ha en 2020. Finalmente, en comparación con 2010, se evidenció una recuperación del 14% en la vegetación media y un 5% en la vegetación alta. Es importante destacar que las imágenes de los años 1989 y 2013 mostraron una presencia significativa de nubosidad, lo que llevó a una subestimación en la clasificación del área para cada tipo de cobertura terrestre.

Palabras clave: Teledetección; minería de oro de aluvión; imágenes satelitales; Landsat, cambio de coberturas terrestres; minería de patrones secuenciales.

Record

Manuscript received: 01/10/2023

Accepted for publication: 26/02/2025

How to cite item:

Herrera, M. M., Fernández, D. S., Vélez, F. J., & Aguirre, N. J. (2025). Temporal analysis of land cover change in Ayapel's alluvial gold mining zones, Colombia. *Earth Sciences Research Journal*, 29(1), 1-13. <https://doi.org/10.15446/esrj.v29n1.111372>

1. Introduction

One of the primary scenarios following the onset of alluvial mining activity is the disappearance of gallery forests, which protect the various water bodies where this activity takes place (Espejo et al., 2018). The absence of vegetation triggers soil degradation and erosion processes, in addition to the loss of various habitats for the animal species that are part of the ecosystem (Bradley, 2020). Deforestation associated with alluvial mining significantly contributes to the degradation of both aquatic and terrestrial ecosystems, impacting biodiversity and soil stability (Donkor et al., 2009; Gerson et al., 2022). The basin of the San Pedro River and the three basins that feed the Ayapel swamp exhibit this condition of deforestation due to mining activity (Pérez-Rincón, 2014). In particular, the Quebradona, Escobillas, and Trejos streams, upstream of the Ayapel swamp, find themselves in a critical situation. Throughout these three basins, the gallery forest has been deforested, and the bed of the streams has been altered (Defensoría del Pueblo, 2015; Rodríguez, 2019).

Similar to other forms of mining, alluvial mining significantly alters the landscape (Dethier et al., 2023), making the monitoring of these changes crucial to quantify the impact of these activities on terrestrial ecosystems. A distinctive procedure of mining in terrestrial placer deposits is the creation of a large pond using mechanical excavators (typically 60 m by 30 m), which is filled with water from a nearby source, referred to as “mining pools.” The excavated material is mixed in the partially filled pond with the added water to form a mineral slurry, which is then washed and filtered for mineral recovery (Ibrahim et al., 2020). The mentioned excavations are generally carried out in places with nearby water bodies, such as streams and rivers, leaving a very particular mark on the landscape as they progress.

On the other hand, remote sensing systems offer extensive opportunities to monitor soils and vegetation, providing an estimation of their characteristics and evolution over time (Dematté et al., 2018). Platforms like Sentinel, Landsat, and Aster provide satellite images and Digital Elevation Models (DEMs), which are essential tools for large-scale real-time monitoring. These platforms offer high accuracy, data authenticity, and comparability, making them widely applied in environmental studies since the 1990s (Wang et al., 2017). The increase in the availability of remote sensing data from these platforms facilitates more frequent map updates, often in near-real time, which is crucial for tracking open-pit mining and recovery efforts (Zhu & Woodcock, 2014). Repeated measurements at regular intervals are needed, and remote sensing often becomes the only alternative to field observations, particularly when historical data is required to study mining and recovery activities (Petropoulos & Partinevelos, 2012).

Sequential pattern mining is a data mining technique aimed at identifying recurring patterns in ordered data, where the temporal or sequential order of events is significant. This method is particularly useful in analyzing large geospatial datasets, such as those derived from remote sensing and environmental monitoring, where patterns evolve over time (Wu & Zhang, 2019). In the context of spatial data, sequential pattern mining helps in detecting spatial and temporal dependencies among events, which can be useful for understanding processes like land-use change, ecosystem dynamics, or mining impacts on the environment (Helmi & Banaei-Kashani, 2016). For instance, spatial sequential patterns can track the progression of deforestation, urban sprawl, or ecological degradation in areas affected by mining, providing insights into how these events unfold across both space and time (García-Gil et al., 2021). This technique has gained notable interest in geospatial studies as it can extract meaningful patterns from complex datasets that traditional methods might overlook (Wu & Zhang, 2019; Tzouramanis, 2018).

In the realm of mining, there are vast opportunities for remote sensing in studying various environmental spheres. In the case of Colombia, the majority of studies monitoring mining areas using this technique have focused on pollution monitoring, aiming to identify impacts of mining activities on water bodies (Quejada Palacios, 2019; Uribe Ospina, 2019), for instance, through the detection of high presence of suspended solids (González, 2015); or impacts on vegetation cover, through measuring the level of forest fragmentation (Anaya & Díaz, 2016; Suarez Prada, 2019). To a lesser extent, research has concentrated on studying coverage changes (Acosta Díaz, 2017), in territorial planning with the zoning of areas with mining potential, considering for its choice, the socio-economic and environmental dynamics (Rodríguez-Luna, 2012), or the monitoring of the restoration of mining areas (Ibrahim et al., 2020; Pérez Umaña, 2018).

Given the vast amount of information obtained from remotely sensed images, it is crucial to apply efficient and computationally less demanding classification and multitemporal analysis methods (Lillesand, Kiefer, & Chipman, 2015). Spectral indices, such as the Normalized Difference Vegetation Index (NDVI) and Enhanced Vegetation Index (EVI), are commonly used in remote sensing to monitor vegetation characteristics and track changes in land cover (McKenna et al., 2020). Various classification methods are employed, with their effectiveness depending on factors such as surface type and application context (Richards, 2013). For example, in the exploration of spatial mosaics, particularly in mining areas, image processing tools like segmentation and unsupervised learning methods, such as K-Means clustering, have been widely used for cover classification (Almeida-Filho & Shimabukuro, 2002; Gillanders et al., 2008).

Spectral indices, such as the NDWI index, developed by McFeeters (1996), is widely used to detect the presence of water bodies and soil saturation. In the mining context, recent studies have employed this index to monitor water quality and the extent of water bodies in areas impacted by open-pit mining (Sulemana et al., 2018). For example, Guo et al. (2019) used NDWI to assess the reduction in the volume of surface water bodies in areas affected by coal mining in China. The study showed that NDWI allowed for the identification of significant decreases in water bodies, correlated with the expansion of mining activities in the region (Guo, Xie, Xu, & Zhang, 2019).

On the other hand, the SAVI index, proposed by Huete (1988), is a modification of the Normalized Difference Vegetation Index (NDVI), designed to correct for soil influence in areas with low vegetation cover. In the mining field, this index has been used to assess vegetation recovery in post-mining rehabilitation areas. A study by Navarro-Cerrillo et al. (2017) used SAVI to analyze the evolution of vegetation in abandoned copper mines in southern Spain. The study found that SAVI provided better discrimination of areas with low vegetation cover, enabling more precise monitoring of ecological regeneration in previously exploited areas (Navarro-Cerrillo, Ruiz-González, Sánchez-Cuesta, & Villar Montero, 2017).

Comparative studies, such as those conducted in arid and semi-arid landscapes, have shown that the SAVI index is more suitable for detecting vegetation in areas with lower vegetation cover and greater soil exposure, a typical scenario in regions affected by open-pit mining (Qi, Chehbouni, Huete, Kerr, & Sorooshian, 1994). For instance, research in the mining region of Jiu Valley, Romania, demonstrated that SAVI can detect vegetation cover at much lower percentages than NDVI, which is crucial for assessing regeneration in post-mining rehabilitation areas (Fernández-Manso, Quintano, & Roberts, 2012). At lower spatial resolutions, SAVI continues to offer greater precision in detecting vegetation compared to NDVI, which tends to saturate or become insensitive in areas with sparse vegetation, as observed in studies using MODIS and Landsat data (Gistec, 2012).

For multitemporal analysis of large geospatial datasets, spatial sequential pattern mining has gained significant attention among researchers (Helmi & Banaei-Kashani, 2016). These techniques aim to extract patterns from transactional frequencies, where each observation—represented as a pixel—contains a sequence of temporally located events. This approach is especially useful for monitoring spatial mosaics, which are critical for studying ecological restoration efforts (Wu & Zhang, 2019)."

This study aimed to monitor the land cover changes of an area located to the south of the Ciénaga de Ayapel, encompassing the Quebradona village, where alluvial gold mining has been present (UNODC, 2019). Monitoring was conducted in the area through the analysis of 10 Landsat TOA images, captured between the years 1985 and 2020. For this purpose, an unsupervised learning classification method was applied, and lastly, a data mining method for the multi-temporal monitoring of coverage changes was utilized.

2. Methodology

2.1. Study Area

The study area consists of a polygon located southeast of the Ciénaga de Ayapel, which houses the Quebradona micro-basin (Figure 1). Ciénaga de Ayapel is located in the department of Córdoba, Colombia. It is part of the larger system of wetlands and alluvial plains known as the La Mojana region and is considered one of the most significant within the floodable system of the San

Jorge River, due to its total area (45 km²) and its importance to the local fishing sector in the local economy (Mejía Ávila et al., 2023). The swamp is classified within a tropical wet forest life zone, with temperatures ranging between 26°C and 28.7°C and average precipitation between 2,000 and 2,500 mm (Ríos et al., 2008). Additionally, it generates surpluses that drain into the San Jorge River, due to its hydrological system. Its average depth is 6 m, and the water level varies up to 4 m between the rainy and dry periods (Ríos et al., 2008). The floodplain basin has a total area of 1,504 km², divided into five micro-basins, among them, the Quebradona micro-basin with an area of 262.14 km² (Serna-lópez & Cañón-barriga, 2020).

In Ayapel, starting around the year 2005, alluvial mining has been carried out intensively and with machinery in the Escobillas, Quebradona, and Trejos streams, which contribute to the swamp (Pérez-Rincón, 2014). The Quebradona micro-basin has been one of the micro-basins most affected by alluvial gold mining. To the north of the Quebradona micro-basin is located the Integrated Resource Management District (DMI) of the Ayapel Wetland Complex, a conservation figure at the national level, of significant importance given that the Ciénaga de Ayapel was declared a RAMSAR site (a figure of wetland conservation at the international level) around the year 2018 (Decree 356 of 2018, Ministry of Environment and Sustainable Development-MADS-).

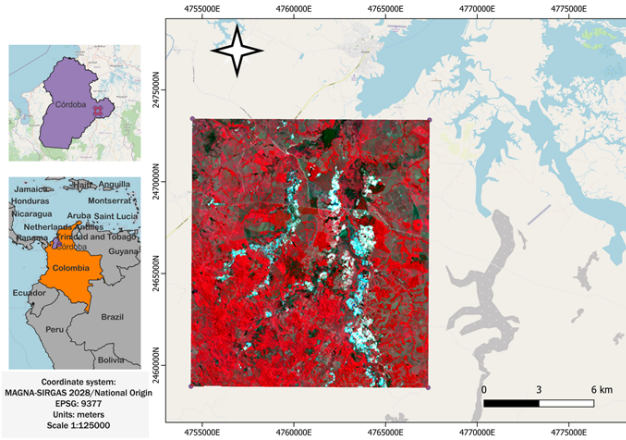


Figure 1. Study area encompassing the Quebradona micro-basin, located in Ayapel, Córdoba. The study area corresponds to the polygon delimited in infrared. In the infrared image, the areas in white and light blue correspond to bodies of water, areas without vegetation, or bare soils.

2.2. Image Acquisition

For this analysis, Landsat T1 images were obtained from the Google Earth Engine database (Gorelick et al., 2017), corresponding to the Landsat 4, 5, and 8 missions, of the study area whose coordinates are shown in Table 1. The downloaded images had atmospheric level preprocessing (TOA), which already have radiometric correction at atmospheric surface level.

Table 1. Coordinates of the study area polygon*.

Latitude	Longitude
8.14645554439919	-75.11254943489037
8.278298734840208	-75.11254943489037
8.278298734840208	-75.2299658167263
8.14645554439919	-75.2299658167263

*The coordinates presented in this table correspond to the polygon drawn in Figure 1.

On the other hand, each Landsat image comes with a set of multispectral bands $\{B_{i,j,1}, \dots, B_{i,j,X}, B_{i,j,QA}\}$, where $B_{i,j,1}$ is the band 1 of the satellite mission corresponding to the image, and $B_{i,j,QA}$ is the Quality Assessment (QA) band, a Landsat product available for cloud detection in the images. Each band $B_{i,j,X}$ is composed of a group of pixels $a_{i,j,X}$, which in the case of TOA images, can take reflectance values between 0 and 1, in the set of real numbers (known as 32-bit floating type in Python); where the index "X" corresponds to the bands used, listed in Table 2.

Table 2. Bands used from the Landsat satellite.

Band	Resolution (m)	Bandwidth (μm)	
		Landsat 4 & 5	Landsat 8
Near Infrared (NIR): $B_{i,j,NIR}$	30	0.76 - 0.90	0.85 - 0.88
Red visible (R): $B_{i,j,R}$	30	0.6 - 0.63	0.64 - 0.67
Green visible (G): $B_{i,j,G}$	30	0.52 - 0.61	0.53 - 0.59

Following the acquisition of the Landsat images, the classification, post-processing, and multi-temporal analysis phases of the study area commenced (Figure 2), with the aim of demonstrating the change in coverages over time. The entire image processing workflow was implemented using Python programming language. A custom software application was developed using Python 3.7.4 (www.python.org) to automate the processing pipeline, ensuring consistent treatment across all selected images. The software is named CATESID, registered by the "Dirección Nacional de Derechos de Autor" filed under number 1-2022-22248. This approach not only standardized the methodology but also significantly enhanced the efficiency and reproducibility of the analysis. The step-by-step methodology employed by the software for processing the satellite imagery is detailed below.

For the first stage "classification", the various bands of the Landsat satellite $\{B_{i,j,1}, \dots, B_{i,j,X}, B_{i,j,QA}\}$ are introduced, and a preliminary classification $C_{i,j,SAVI}$ is obtained based on the Soil Adjusted Vegetation Index (SAVI). This index was used because it showed good distinction between cover types. Each class or soil coverage was chosen according to the types of coverage observed in the field and in RGB satellite images, but these classifications were further validated using the Soil Adjusted Vegetation Index (SAVI) to ensure accuracy. The SAVI, which adjusts for soil brightness and is more effective in areas with sparse vegetation (Huete, 1988), was used to determine vegetation levels. According to the SAVI values, low vegetation corresponds to values near 0, medium vegetation ranges between 0.2 and 0.5, and high vegetation is represented by values greater than 0.5 (Huete, 1988). These SAVI-derived categories were used to cross-check the initial classifications, ensuring consistency and providing a clearer distinction between areas of low, medium, and high vegetation cover (Huete, 1988; Qi et al., 1994).

Subsequently, the "post-processing" phase begins where the classified image obtained in the previous stage is entered, and additionally a raster-type image $V_{i,j,W}$ obtained from the vectorization of rivers and streams is entered. The vectorization was carried out in ArcGIS (Version 2.15) (Esri, 2020) using an image of the study area and a Digital Elevation Model (DEM) (Moore, et al., 1991), this image, taken in 1985, was compared to a more recent image from 2020. The comparison revealed no significant differences in the course of the water networks. Additionally, this information was cross-referenced with the hydrological network recorded in regional maps. In this phase, new classes such as the "Clouds" class, the "Water" class, and the "Mining Soil" class are added, obtaining the classified image $C_{i,j}$. In the "Water" class, the Normalized Difference Water Index-NDWI- (McFeeters, 1996) was used to identify "small bodies of water" or "mining pools" which in turn are useful to delimit active mining areas (Ibrahim et al., 2020), this methodology is explained later. To evaluate the classification accuracy, it was employed established methods including confusion matrices and visual interpretation techniques (Congalton & Green, 2019; Foody, 2002; Olofsson et al., 2014). The assessment was performed using ArcGIS Accuracy Assessment tools, incorporating the Kappa coefficient to measure classification-reference agreement (Cohen, 1960; Esri, 2023). Finally, for the "multi-temporal analysis", a set of images $\{C_{i,j,1}, \dots, C_{i,j,t}\}$ are introduced, where t refers to a specific capture date for the image, and where $C_{i,j,1}$ is an $m \times n$ matrix, and each pixel i, j has a number equivalent to a coverage class as its value; in this set of input images, the "Clouds" class is excluded since it is considered as an information void. After applying the *Sequential Pattern Discovery using Equivalence Classes* (SPADE) method (Zaki, 2001), "Sup" support values and "Conf" confidence values are obtained for each of the sequences found by the method, understanding a sequence as an ordered set of classes. The definition of land cover classes or types was validated through field observations that were accurately georeferenced and compared with the pixels in the satellite image. In total, eight points were chosen at random and in such a way that the three levels of vegetation

cover (high, medium, and low) could be validated, in addition to bare soil cover (as is showed in Figure 2). Identifying additional field points was not possible due to limited access to the area for security reasons. Additionally, conversations were held with residents about land cover changes over time and significant socioeconomic events in the area throughout the years.

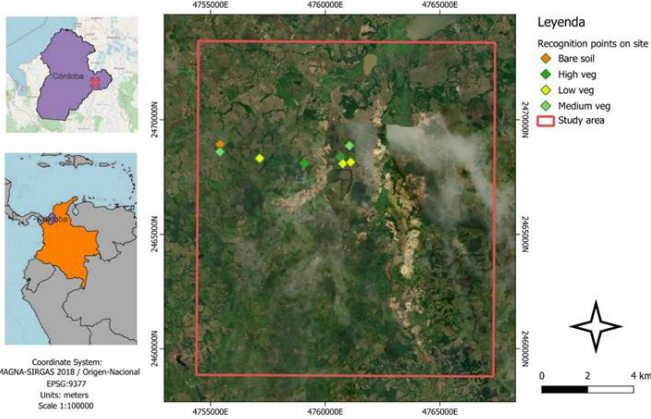


Figure 2. Field survey points representing observed land cover types, categorized into distinct classes.

Regarding the measurement of classification accuracy, the total overall accuracy was calculated as the average of the overall accuracies provided by each of the classified images. The accuracy assessment was conducted following the principles established by Congalton and Green (2019), employing a confusion matrix (Foody, 2002) and visual interpretation techniques (Olofsson et al., 2014). The process was implemented in ArcGIS (Version 2.15) (Esri, 2020) using the Accuracy Assessment tools (Esri, 2023), which include the calculation of the Kappa coefficient (Landis & Koch, 1977) to evaluate the agreement between the classification and the reference data.

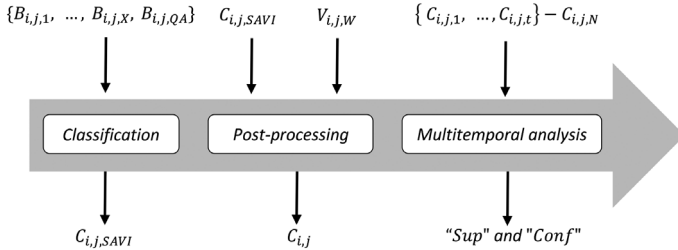


Figure 3. Summary of phases for satellite image processing.

The following is a more detailed explanation of each of the stages illustrated in Figure 3

2.3. Classification

Prior to applying unsupervised classification, the Soil Adjusted Vegetation Index (SAVI) was calculated for each satellite image, as described in Figure 4. This index applies a correction for the presence of bare soil, yielding good results for areas with this characteristic (Huete, 1988). In this way, $B_{i,j,SAVI}$ is obtained, calculated as shown in equation (1).

$$B_{i,j,SAVI} = \frac{B_{i,j,NIR} - B_{i,j,R}}{B_{i,j,NIR} + B_{i,j,R} + L} (1 + L) \text{ con } L = 0.5 \quad (1)$$

In this case, parameter L was chosen as 0.5 given that the study area exhibits a moderately exposed surface due to the presence of bare soil. This

value is also commonly recommended for most soil types (U.S. Geological Survey, n.d.).

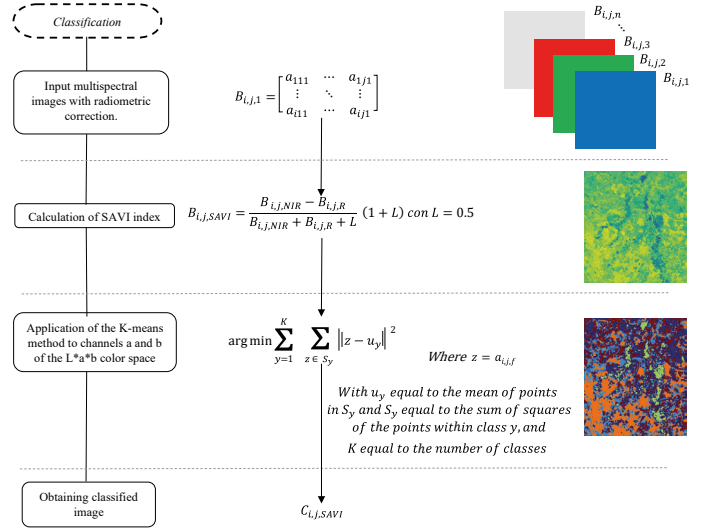


Figure 4. Description of satellite imagery classification phase.

Subsequently, once it was observed that the SAVI index presented a good delimitation of coverages, especially of bare soil, moderate, medium, and high vegetation. In this classification, the “high vegetation” class corresponds to dense forests characterized by mature vegetation. The “medium vegetation” class encompasses sparse forests and established crop areas. The “low vegetation” class is representative of grasslands and recently planted agricultural fields. The conversion from RGB color space to Lab color space was proceeded, applying only the unsupervised classification by the K-means method (2) to channels a and b, discarding the L channel corresponding to luminosity. From the unsupervised classification, a good delimitation of the mentioned classes () was obtained, later supervised classification of the classes delimited by the classification method was performed, indicating to which class a certain coverage color corresponded.

$$\arg \min \sum_{y=1}^K \sum_{z \in S_y} \|z - u_y\|^2 \text{ with } z = a_{i,j,B_{SAVI}} \quad (2)$$

In equation (2), corresponding to the definition of the K-means method (Hartigan & Wong, 1979), given a set of observations $a_{i,j,B_{SAVI}}$, which corresponds to the set of pixels that form each image $B_{i,j,SAVI}$, K-means constructs a partition of observations into K clusters, where K is equal to the total number of classes, in order to minimize the sum of squares within each cluster y , where y refers to each class. Additionally, u_y is equal to the mean of points in S_y , where S_y is equal to the sum of squares of the points within class y . From this classification process, a classified image $C_{i,j,SAVI}$ is obtained, where for each $a_{i,j}$ there is a label of one of the classes y . The class y , up to the point of the application of unsupervised classification, can take values corresponding to the labels “Bare Soil”, “High Vegetation”, “Moderate Vegetation”, and “Low Vegetation”. Although K-means has certain precision limitations compared to other methods, its simplicity and the generally satisfactory results achieved in this study made it the chosen approach. Furthermore, since the delimitation carried out by the SAVI index already left some well-identified contrasts, it was sufficient to apply a cluster to delimit these contrasts into classes.

2.4. Post-processing

Following the classification of the images, additional post-processing was carried out to include some classes, such as water (including the hydrological

network), clouds, and active mining areas. For the identification of water bodies, the NDWI (3) was utilized, from which a raster file $B_{i,j,NDWI}$ is derived, with its pixels taking real values ranging between -1 and 1.

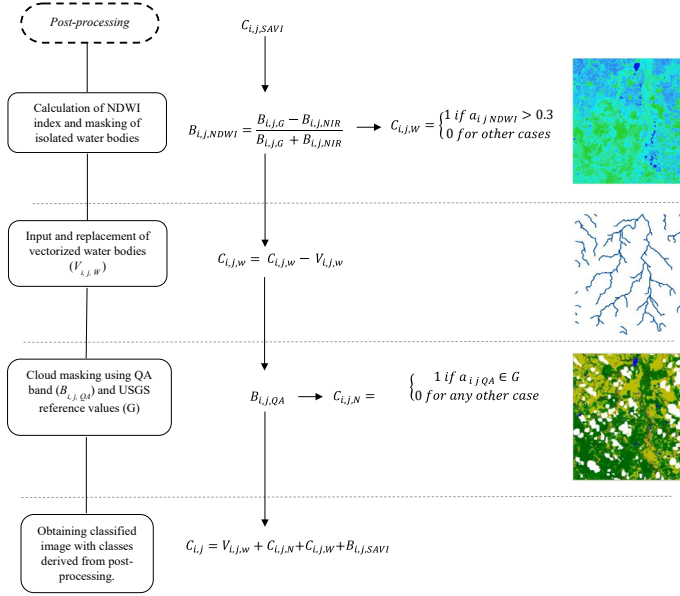


Figure 5. Description of the post-processing phase.

The NDWI was developed to delineate open water features and enhance their detection in remote sensing digital imagery. Utilizing the Near Infrared (NIR) and visible Green Light (G) spectral bands, the NDWI effectively aids in identifying such features while mitigating interference from vegetation and ground surface characteristics (McFeeters, 1996).

$$B_{i,j,NDWI} = \frac{B_{i,j,G} - B_{i,j,NIR}}{B_{i,j,G} + B_{i,j,NIR}} \quad (3)$$

Following the process, a water mask, denoted as $C_{i,j,W}$, was created. This mask assigned a value of 1 to each pixel that satisfied the condition of having an NDWI value greater than 0.3, and assigned 0 for any other case, as expressed in equation (4).

$$C_{i,j,W} = \begin{cases} 1 & \text{if } a_{i,j,NDWI} > 0.3 \\ 0 & \text{for any other case} \end{cases} \quad (4)$$

Having obtained the water class mask $C_{i,j,W}$, a raster file with vectorized water bodies $V_{i,j,W}$ was loaded, which came from a process in the ArcGIS software (Version 2.15) (Esri, 2020) of an image from a Digital Elevation Model (DEM) sourced from the ASTER satellite. Subsequently, a subtraction operation was carried out between the files $C_{i,j,W}$ and $V_{i,j,W}$, so that only the pixels corresponding to isolated water bodies remained in the mask $C_{i,j,W}$. With the isolated water bodies, that is, those that do not correspond to natural water bodies like streams and rivers, a conditional operation was applied for the identification of mining pools, which typically measure between 30 and 60 m² (Ibrahim et al., 2020). This was done with the aim of identifying bare soil around that might correspond to an active mining area, thereby distinguishing between the "Bare soil" class and the "Active mining" class, in accordance with the methodology applied by Ibrahim et al. (2020).

Lastly, regarding cloud identification, the band $B_{i,j,QA}$ was utilized, with which a comparison is made against a set of reference values G provided by the USGS for the band $B_{i,j,QA}$, that enables determining whether a pixel value of said band corresponds to a cloud. Therefore, a cloud mask $C_{i,j,N}$ was obtained, corresponding to the "Cloud" class calculated as shown in equation (5), where a value of 1 is assigned to the pixel whose value falls between the reference values G , and 0 for any other case. Thus, in the end, an image $C_{i,j}$ with class

values and additional ones, such as "Water", "Active mining", and "Clouds" is obtained, as shown in equation (6).

$$C_{i,j,N} = \begin{cases} 1 & \text{if } a_{i,j,QA} \in G \\ 0 & \text{for any other case} \end{cases} \quad (5)$$

$$C_{i,j} = V_{i,j,W} + C_{i,j,N} + C_{i,j,W} + C_{i,j,SAVI} \quad (6)$$

2.5. Multitemporal Analysis

For the multitemporal analysis phase, a set of images $C_{i,j}$, denoted as $\{C_{i,j,1}, \dots, C_{i,j,t}\}$, was utilized, where the subscript t corresponds to an image from a specific date, for the computation of a sequence matrix $S_{i,j}$ (Figure 6), which contains $y_{i,j}$ with t layers, through the SPADE method.

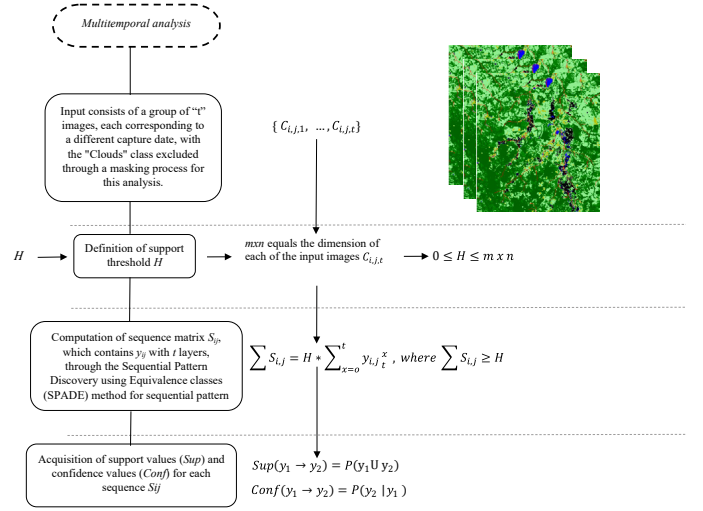


Figure 6. Summary of the multitemporal analysis phase.

A sequence refers to a chronologically ordered list of classes, where there exists a sequence of classes for each point $a_{i,j}$ in the matrix. Therefore, given a threshold of minimum occurrence H for a sequence S , the number of resulting sequences is defined as (7). Additionally, $0 < H \leq mxn$ with mxn being the dimensions of each of the input images $C_{i,j,t}$. This method detects a sequence for every $a_{i,j}$ across the t layers; however, only the sequences whose support or probability of occurrence is greater than or equal to the defined threshold H prevail (Wu & Zhang, 2019).

$$\sum S_{i,j} = H * \sum_{x=0}^t y_{i,j,t}^x, \text{ where } \sum S_{i,j} \geq H \quad (7)$$

In the end, a set of sequences is obtained, each with a support value "Sup" and confidence value "Conf". Support is defined as the percentage of appearance of a certain sequence, in relation to the total number of sequences (8), and confidence corresponds to the fraction between the number of appearances of a certain sequence, in relation to the total number of observations that initiated with a specific reference class (9).

$$Sup(y_1 \rightarrow y_2) = P(y_1 | y_2) \quad (8)$$

$$Conf(y_1 \rightarrow y_2) = P(y_2 | y_1) = \frac{P(y_1 | y_2)}{P(y_1)} \quad (9)$$

In this way, the support reflects the percentage of appearances of a sequence in relation to the total pixels of each image ($m \times n$), and confidence refers to the percentage of appearances of a specific sequence in relation to the total pixels that initiated with a reference class, that is, the first class of the sequence, also known as the antecedent.

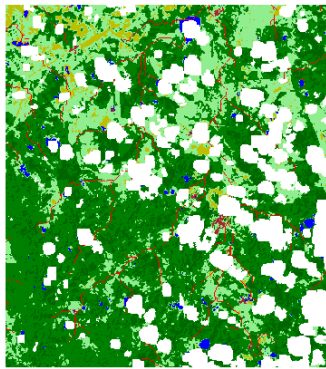
3. Results and discussion

3.1. Classification Accuracy Results

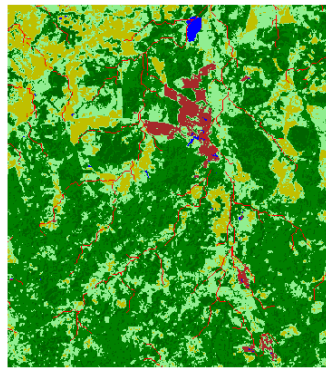
The classification performed using the SAVI index, image processing, and the unsupervised classification method K-means yielded an overall accuracy of $74.37\% \pm 0.10$ and a Kappa coefficient of 0.658. According to Landis and Koch (1977), a Kappa coefficient between 0.61 and 0.80 indicates substantial agreement, suggesting that the classification is of good quality. However, other studies have reported higher overall accuracies and Kappa

coefficients, depending on factors such as the resolution of the images used and the classification method employed. For example, in the classification of SPOT images (which have higher resolution than Landsat) for land cover analysis, an overall accuracy of 94.61% and a Kappa coefficient of 0.92 were obtained (Duarte et al., 2017). Additionally, other classifications using algorithms such as Random Forest (RF), Support Vector Machine (SVM), Artificial Neural Network (ANN), Fuzzy Adaptive Resonance Theory Mapping (Fuzzy ARTMAP), Spectral Angle Mapper (SAM), and Mahalanobis Distance (MD) reported Kappa coefficients ranging from 0.82 for MD to 0.89 for RF (Talukdar et al., 2020). While in general, other algorithms may improve classification accuracy, the result obtained with K-means combined with the SAVI index yielded acceptable results for this study.

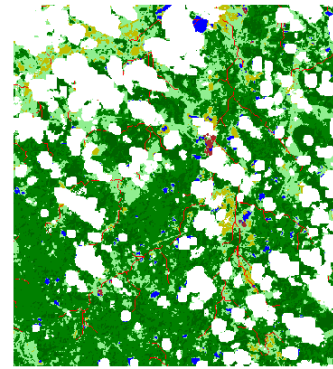
In this study, it was observed that Landsat 4 and 5 images showed lower accuracy compared to Landsat 8 images. This disparity is likely due to the improved radiometric resolution of Landsat 8, which facilitates better differentiation of land cover classes and, consequently, more accurate classification.



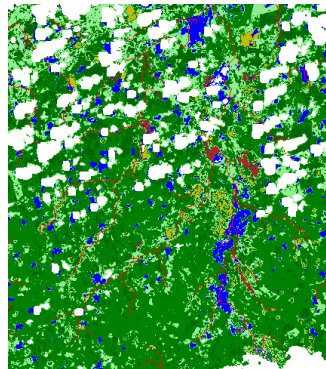
(a) 24/01/1985



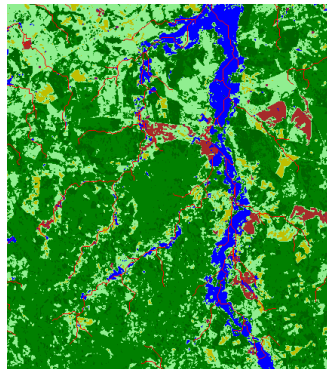
(b) 30/01/1987



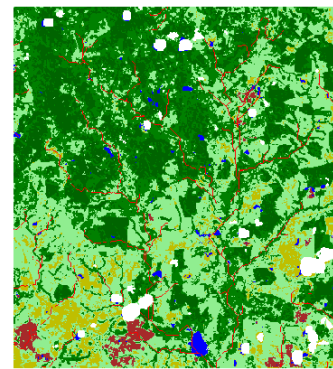
(c) 11/01/1989



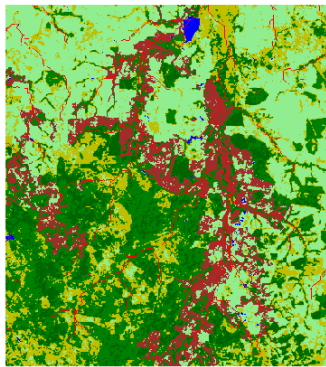
(d) 20/07/1991



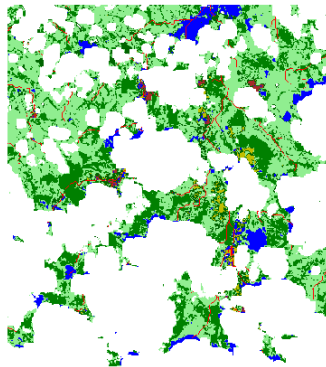
(e) 17/07/1996



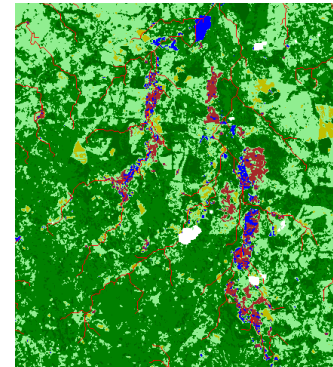
(f) 05/02/2001



(g) 29/01/2010



(h) 23/12/2013



(i) 19/07/2014

(Continued)

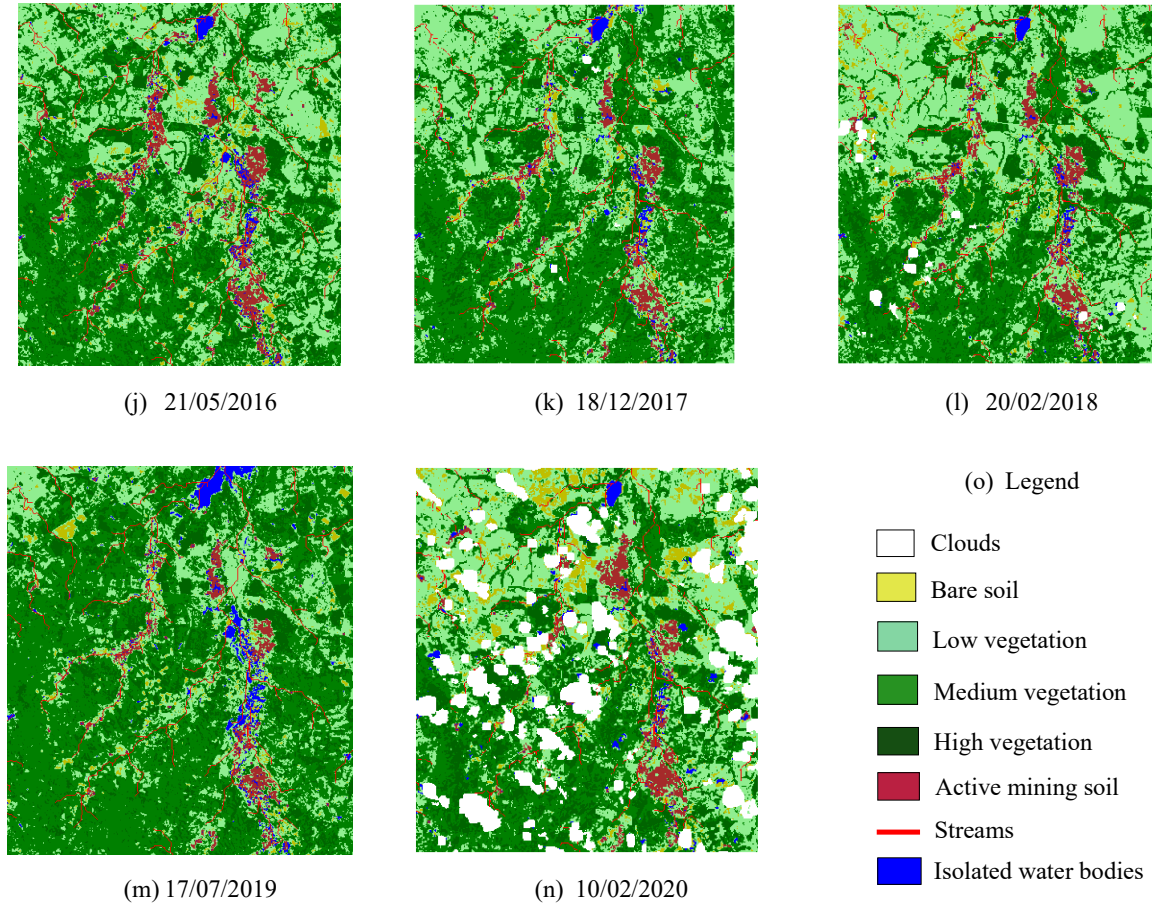


Figure 7. Classified Landsat images resulting from the post-processing stage (all images have the same scale).

3.2. Soil Cover Classification Analysis from Landsat Images.

For the study area, the classification of images corresponding to dates between 1985 and 2020 was obtained, as can be seen in the figure below (Figure 8).

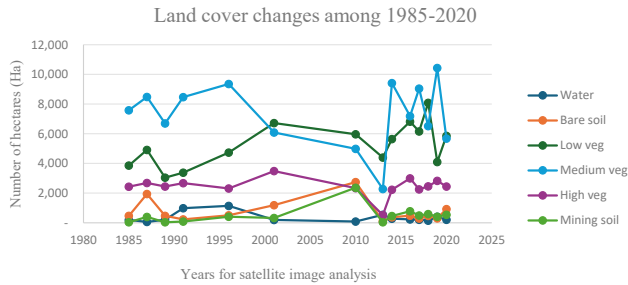


Figure 8. Classification of land cover between 1985 and 2020.

Based on the classification of the images and the graph showing the behavior of the different classes over time, a general decrease is observed across all classes for the images from 1989 and 2013, which exhibit significant cloud cover. Therefore, this decrease in the area of the classes is more likely attributed to the presence of clouds rather than an actual reduction in the area occupied by each class. A similar pattern is observed for the years 1991 and 2020, although to a lesser extent, due to the reduced cloud cover in these images compared to the ones mentioned earlier (Table 3).

Table 3. Percentage of gain and loss of coverage based on the classification made.

Year	Water (%)	Bare Soil (%)	Low Vegetation (%)	Medium Vegetation (%)	High Vegetation (%)	Active Mining Soil (%)
1985	-	-	-	-	-	-
1987	-67.93	313.04	27.35	11.78	10.18	830.36
1989	244.1	-76.08	-38.04	-21	-8.71	-91.21
1991	362.01	-50.09	11.22	26.35	9.03	146.49
1996	16.33	120.51	39.78	10.57	-13.3	387.46
2001	-83.35	131.3	42.11	-34.92	50.59	-21.25
2010	-55.84	131.72	-11.2	-18.25	-33.07	622.07
2013	543.04	-96.05	-26.39	-54.26	-77.61	-98.14
2014	-48.68	246.31	28.54	313.16	327.13	932.31
2016	-16.87	27.49	20.63	-23.63	34.29	71.81
2017	-10.46	-39.1	-9.63	25.82	-24.61	-36.87
2018	-26.2	61.79	0.05	-27.89	9.05	20.44
2019	166.92	-34.57	-33.4	60	14.67	-31.39
2020	-50.17	199.97	42.84	-45.6	-13.39	33.93

Based on Figure 8, it can be observed that medium vegetation predominates in the area compared to tall vegetation. Over the years, low vegetation has shown an increasing trend, while medium and tall vegetation experienced a decline starting in 1996, stabilizing again in 2014. It is important to note that the decrease in hectares across all classes in 2013 is primarily due to the presence of clouds in the image for that year.

Regarding active mining land and bare soil, an increase in hectares is evident starting in 1996, possibly related to the reduction of tall and medium vegetation caused by deforestation during the same period. However, these land covers (active mining land and bare soil) began to decrease after 2010, which could be associated with the increase in medium and tall vegetation observed from 2014, due to the revegetation of areas abandoned by mining activities. This observation is consistent with natural revegetation processes and potential restoration efforts in post-mining landscapes, as documented by Gastauer et al. (2019) in similar tropical environments. In the study area, some assisted restoration attempts were observed.

On the other hand, active mining soil and bare soil seem to exhibit very similar behavior in their changes over time. This can also be seen in the classification matrix in Figure 9 which yielded a positive rating of 0.76, which implies a good correlation between classes. It could be inferred that as the amount of bare soil increases, the number of active mines also rises, since stripping the soil of its vegetative cover is the initial step for the onset of extractive activity. Additionally, according to residents, all areas devoid of vegetative cover correspond to active mining areas. This relationship between active mining areas and bare soil dynamics aligns with findings from Chica-Olmo et al. (2021), who analyzed land cover changes in mining regions of Southern Spain and observed a strong correlation between the expansion of bare soil and increased mining activities over a 30-year period. Similarly, Sonter et al. (2017) documented in their study of Brazilian Amazon mining areas that the removal of vegetation directly precedes the establishment of mining operations, creating extensive zones of bare soil. These studies highlight how bare soil serves as both an indicator and a precursor of active mining operations.

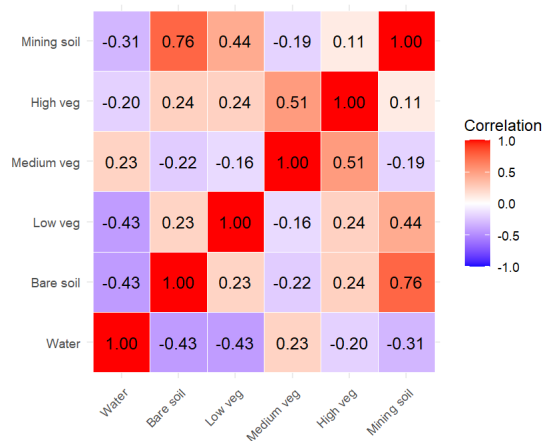


Figure 9. correlation matrix between classes after classification between the years 1985 and 2020.

The spatial distribution of high and medium vegetation classes reveals certain similarities in their occurrence patterns, as observed in Figure 7 and the correlation matrix (Figure 9). These two classes exhibit a positive correlation of 0.51, indicating that years with significant high vegetation cover often also show a notable presence of medium vegetation. This co-occurrence may reflect the complex structure of forest ecosystems during various stages of growth or recovery, as highlighted by Chazdon (2014) in studies on tropical forest regeneration.

Within the study area, medium vegetation emerges as the most prevalent cover type, followed by low vegetation and high vegetation. This pattern is evident in Figure 8, where medium vegetation averaged 7,300 hectares, low vegetation 5,261 hectares, and high vegetation 2,436 hectares across all analyzed years. This distribution highlights a landscape mosaic dominated by intermediate stages of vegetation growth or regrowth, a characteristic feature of tropical regions undergoing land-use changes (Arroyo-Rodríguez et al., 2017).

It's important to note that these observations are based on spatial patterns and relative abundances derived from our classification results. Further statistical analysis and ground validation would be necessary to establish any definitive relationships or trends among these land cover types.

Regarding the behavior of active mining over the years (Figure 9), it can be observed that initially, in the year 1987, there was an increase in mining activity of 351.9 ha compared to 1985; that is, there was an increase of 9 times more compared to what there was in 1985, a trend consistent with the data collected in the field through interviews with local populations. They confirm that between 1987 and 1988, there was an increase in mining activity due to the incorporation of machinery in gold mining, a method not used in previous years, where mining practices were more artisanal.

Based on field interviews, gold mining activity in Ayapel was relatively low between the 1990s and 2004. This was attributed to the presence of illegal armed groups that controlled mining operations, discouraging extensive participation by the local population. This behavior, as described by local residents, aligns with scientific evidence demonstrating a significant relationship between armed conflict, its impact on natural resources, and the transformation of ecosystems in Colombian territories (Salazar et al., 2018).

Figure 9 shows an increase in mining activity between 2001 and 2010, amounting to 2,039 hectares. However, during this period, Landsat imagery was unavailable due to a "striping" issue with the satellite, leaving uncertainties about the fluctuations in mining activity during this time. According to field interviews, mining activity increased significantly after 2005, coinciding with the demobilization of armed groups that had previously controlled the region. This shift allowed both civilians and other criminal organizations to take over mining operations. The use of machinery and more advanced methods compared to traditional techniques enabled faster and more extensive resource extraction, leading to a significant expansion of mining areas. According to Figure 10, by 2014, mining areas decreased compared to 2010.

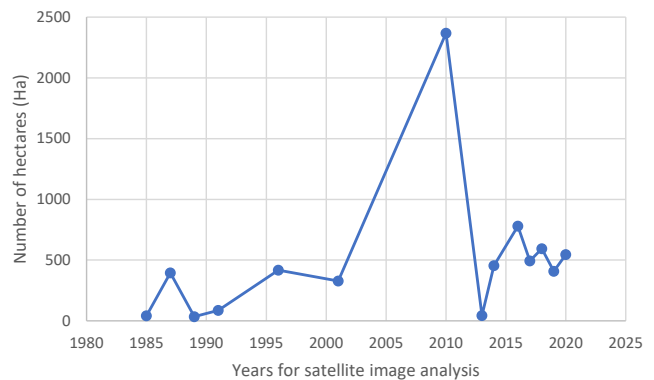


Figure 10. Change in hectares of active mining soil over time.

Although a correlation between mining activity and vegetation cover might theoretically be expected, the correlation matrix in Figure 9 shows no significant relationship between active mining areas and vegetation types. This lack of correlation could be attributed to several factors. One of them is that satellite image classification may be affected by errors related to image resolution, atmospheric conditions, or limitations in classification algorithms, which impact the accuracy of the data obtained. Computational methods have proven to be fast, accurate, and cost-effective tools for automatic land-use classification in satellite imagery (Gómez & Perea, 2017). Finally, a limited number of available images for analysis may fail to capture the temporal and spatial variability of mining activities and their impact on vegetation, particularly in regions with high cloud cover, where cloud-free imagery is essential for accurate monitoring. Therefore, the observed lack of significant correlation suggests the need for improved classification techniques and an expanded image database for future studies.

3.3. Seasonal Multitemporal Analysis

Based on the methodology of Ibrahim et al. (2020), for the seasonal analysis, images from the years 2016, 2017, 2018, 2019, and 2020 were chosen, from the months of May, December, February, July, and February respectively. The images from 2016 and 2019 correspond to the rainy season in the study area and the images from the years 2017, 2018, and 2020 correspond to the dry season. This sequential pattern mining analysis yielded the sub-sequences shown in Table 4.

The analysis from Table 4 reveals that the subsequence Mining Soil->Mining Soil had the highest occurrences with 6081, reflecting a 58.71% confidence that areas classified as mining soil in one year remained so in the following year. There is 60% confidence that such areas from 2016 remained mining soil through 2019. Other notable subsequences include Active Mining Soil -> Low Vegetation and Active Mining Soil -> Low Vegetation -> Low Vegetation, with occurrences of 4969 and 2953, and confidence levels of 47.97% and 59.42% respectively. This suggests a 40 to 60% probability of areas transitioning from Mining Soil to Low Vegetation, comparable to the probability of remaining as Mining Soil.

Table 5 illustrates sequences initiated with vegetation classes. The most recurrent sequence was Vegetation High->Vegetation High, indicating that most high vegetation forest remained constant over the analyzed period. There is a notable increase in vegetation during the rainy season compared to the dry season, due to better growth conditions in winter. Moreover, in the dry season, grasslands tend to decrease or get replaced by crops with the arrival of rains. The results also show a tendency to maintain the same vegetation classification between the years 2017 and 2018.

In Table 5, the blue color alludes to the winter season and the orange color refers to the dry season. Lastly, the arrows indicate an increase in vegetation with the transition from the dry season to the rainy season.

3.4. Annual Multitemporal Analysis.

Based on the methodology of Ibrahim et al. (2020), the annual multitemporal analysis grouped images from 1985 to 2014 into subgroups for better visualization and interpretation of sequences, based on classification results. Three subgroups were formed: 1985-1989, 1989-2001, and 2001-2014, selected based on the variation behavior in vegetation and mining areas between image dates. This facilitated the interpretation of the annual behavior in vegetation and mining activity over time.

About the sequences of the years 1985, 1987, and 1989 (Table 6), the most occurring sequences were High Vegetation->Medium Vegetation->Medium Vegetation, with an occurrence of 29964 and a confidence of 0.4161. This means that the pixels classified as high vegetation had a 41.61% probability of being reclassified as medium vegetation, which would imply a loss of dense forest during this period.

Table 4. Subsequences initiated with the class “Mining soil” in the image of 2016.

2016	2017	2018	2019	Occurrence	Support	Confidence
Minning soil	Bare soil			2819	0.01349	0.27218
Minning soil	Low veg			4969	0.02377	0.47977
Minning soil	Low veg	Low veg		2953	0.01413	0.59428
Minning soil	Minning soil			6081	0.02909	0.58714
Minning soil	Minning soil	Minning soil		4077	0.01950	0.67045
Minning soil	Minning soil	Minning soil	Minning soil	2481	0.01187	0.60854

Table 5. Sequences for seasonal analysis of vegetation type.


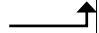

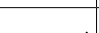
21/05/2016	18/12/2017	20/02/2018	17/07/2019	10/02/2020	Occurrence	Support	Confidence
High veg	High veg	High veg 	High veg	High veg	35904	0.171	0.620
Low veg	Medium veg	Low veg 	Medium veg	Low veg	7047	0.033	0.585
Medium veg	Medium veg	Low veg 	Medium veg	Low veg	6545	0.031	0.507
Low veg	Low veg	Low veg 	Medium veg	Low veg	5757	0.027	0.572
Medium veg	Medium veg	Medium veg	High veg	Medium veg	3695	0.017	0.449
High veg	High veg	High veg	High veg	Medium veg	3472	0.016	0.060
Medium veg	Low veg	Low veg	Medium veg	Low veg	3465	0.016	0.583

Table 6. Sequences of Vegetation classes for the years 1985, 1987, and 1989.

1985	1987	1989	Occurrence	Support	Confidence
High veg	Medium veg	Medium veg	29964	0.143	0.416
High veg	Low veg	Medium veg	7805	0.037	0.307
Low veg	Low veg	Medium veg	7201	0.034	0.190
Low veg	Low veg	Low veg	6999	0.033	0.185
High veg	Medium veg	High veg	6835	0.032	0.094
Medium veg	High veg	High veg	5045	0.024	0.177
Low veg	Bare soil	Low veg	4830	0.023	0.360

Table 7. Subsequences of “Mining Soil” and “Bare Soil” classes for the years 1989, 1991, and 1996.

1989	1991	1996	Occurrence	Support	Confidence
Low Veg	Bare soil		10873	0.052	0.087
Medium Veg	Bare soil		8734	0.041	0.053
Bare soil	Low veg		8609	0.041	0.380
Mining soil	Low veg		3340	0.015	0.379
Bare soil	Bare soil		3190	0.015	0.141
Medium veg	Mining soil		3041	0.014	0.018
Bare soil	Low veg	Low veg	2749	0.013	0.319
Bare soil	Medium veg		2739	0.013	0.121

Table 8. Sequences and Subsequences of Classes for the Years 2001, 2010, 2013, and 2014.

2001	2010	2013	2014	Occurrence	Support	Confidence
Low veg	Low veg		Medium veg	11881	0.056	0.621
Low veg	Bare soil		Low veg	4335	0.020	0.522
Low veg	Bare soil	Medium veg	Medium veg	4229	0.020	0.350
High veg	High veg		Medium veg	4036	0.019	0.371
Medium veg	Low veg	Medium veg	Medium veg	4003	0.019	0.234
Low veg	Mining soil		Medium veg	3947	0.018	0.535
Low veg	Mining soil	Medium veg	Medium veg	3802	0.018	0.363
Low veg	Bare soil		Medium veg	3488	0.016	0.420
Low veg	Bare soil	Medium veg	Low veg	3282	0.015	0.271
High veg	High veg	High veg	High veg	2965	0.014	0.207
High veg	Veg media		High veg	2875	0.013	0.293
High veg	Low veg		Medium veg	2516	0.012	0.715
Low veg	Mining soil		Low veg	2428	0.011	0.329

Another notable sequence is Vegetation low → Bare soil → Vegetation low, with an occurrence of 4830 and a confidence of 0.3604, indicating that there was a 36.04% probability that pixels classified as low vegetation, would be reclassified as bare soil. This could be interpreted as an increase in mining activity between 1985 and 1987, and a subsequent decline in activity between 1987 and 1989, which aligns with the presence of outlaw groups in the territory and their influence on the behavior of this activity.

The study analyzes the period between 1985–2020, noting a similar trend between “Mining Soil” and “Bare Soil” classes due to their inherent relationship. Particularly in 1989, 1991, and 1996, an increase in mining activities is observed, corroborated by multitemporal analysis results (Table 7). Table 7 shows prevalent sub-sequences: Low Vegetation → Bare Soil and Medium Vegetation → Bare Soil. Despite high occurrence, these sequences exhibit low confidence levels, due to vegetation transitioning to other classes, in sync with the increased medium vegetation noted in classification results. Interestingly, sequences beginning with Mining Soil and Bare Soil classes showed a tendency to transition into Medium and Low Vegetation classes during 1991 and 1996, hinting at a potential vegetation recovery phase with a 40% probability of transitioning from mining or bare soil to vegetated soil.

The multitemporal analysis conducted for the images of the years 2001, 2010, 2013, and 2014 revealed the subsequence “Low Vegetation → Low Vegetation → Medium Vegetation” with the highest number of occurrences (11881) and a confidence level of 62% (Table 8). This suggests an increase in medium vegetation from low vegetation, with a 62% probability that the “Low Vegetation” class from 2010 would become “Medium Vegetation” in 2014.

On the other hand, sequences that started with the “Low Vegetation” class in 2001 and transitioned to “Bare Soil” in 2010 tended to classify as “Medium Vegetation” or “Low Vegetation” in 2013 and 2014, with a probability ranging from 30% to 50% of exhibiting this behavior. Additionally, the “Low Vegetation” class in 2001 showed a probability of 30% to 53% of becoming “Mining Soil” in 2010 and “Medium Vegetation” or “Low Vegetation” in the subsequent years (2013 and 2014). These results are aligned with the analysis based on the classification of the images, indicating an increase in mining activity from 2001 to 2010 and a decrease in activity by 2014.

Conclusions

The classification accuracy achieved using the k-means method and certain spectral indices in this study was lower compared to other currently available methods for remote sensing of land cover. However, the results were acceptable, with an overall accuracy of $74.37\% \pm 0.10$ and a Kappa coefficient of 0.658. One limitation that introduced a degree of error in the classification was the presence of cloud cover, which led to an underestimation of the hectares classified within the different land cover types. Nevertheless, this underestimation was accounted for in the analysis of the results. Finally, the accuracy of the land cover classification was influenced not only by the classification method employed but also by the resolution of the images, as higher resolution results in greater precision in delineating land cover types.

According to the results obtained in the classification process, mining in Ayapel has increased in recent years, particularly since 2016, although not to the same extent as the exponential growth observed between 2000 and 2013. It can also be concluded that significant revegetation occurred between the 1990s and 2000s, and again between 2013 and 2020, indicating that vegetation restoration has taken place in mining areas, provided there is a cessation in the intensity and occurrence of mining activity. Given the observed increase in revegetation when mining activity ceases, it is essential to implement ecological restoration programs in areas where mining has decreased or stopped. This includes activities such as planting native species of high and medium vegetation cover, which are key to restoring the ecosystem's structure and function (MDPI, 2023). Additionally, it is crucial to limit the expansion of mining into new areas through zoning policies that define mining exclusion zones in areas of high ecological importance, such as those with dense vegetation or critical functions for biodiversity and the hydrological cycle.

On the other hand, regarding the changes in coverage, the multitemporal analysis from 2016 to 2020 shows that areas initially classified as “Mining soil” exhibit two main trends: a significant persistence as mining soil over the years, which is consistent with areas of ongoing exploitation, and a notable transition to “Low veg” (low vegetation), possibly associated with partial recovery processes or the abandonment of mining areas. On the other hand, transitions to other classes, such as “Bare soil,” are less common. This suggests that mining

activities dominate over time, although there are some indications of limited ecological regeneration in certain cases.

Acknowledgments

This research was conducted as part of the project “SIIU 2020-37870: System for the Recording and Monitoring of Environmental Variables in the Ciénaga de Ayapel.

References

- Acosta Díaz, D. M. (2017). *Estudio multitemporal de la dinámica de explotación de oro de aluvión del Bajo Cauca Antioqueño en los años 2014 y 2017 a través de imágenes satelitales*. Universidad Militar Nueva Granada.
- Agencia Nacional de Minería (ANM). (2019). *El título minero y sus etapas*. Recuperado de <https://www.anm.gov.co/?q=content/el-titulo-minero-y-sus-etapas>.
- Almeida-Filho, R., & Shimabukuro, Y. E. (2002). Digital processing of a Landsat-TM time series for mapping and monitoring degraded areas caused by independent gold miners, Roraima State, Brazilian Amazon. *Remote Sensing of Environment*. [https://doi.org/10.1016/S0034-4257\(01\)00237-1](https://doi.org/10.1016/S0034-4257(01)00237-1)
- Anaya, L., & Díaz, A. (2016). Análisis de la fragmentación de coberturas naturales producida por la minería a cielo abierto en el Municipio La Jagua de Ibirico, Cesar. *Journal of Chemical Information and Modeling*, 54.
- Arroyo-Rodríguez, V., Melo, F. P., Martínez-Ramos, M., Bongers, F., Chazdon, R. L., Meave, J. A., ... & Tabarelli, M. (2017). Multiple successional pathways in human-modified tropical landscapes: new insights from forest succession, forest fragmentation and landscape ecology research. *Biological Reviews*, 92(1), 326-340
- Borrero Morales, N. (2014). Aluvión: a cielo abierto. *Semana Sostenible*. Recuperado de <https://www.semana.com/medio-ambiente/multimedia/mineria-aluvion-cielo-abierto/32234/>
- Bradley, S. (2020). Mining's impacts on forests. Chatham House. <https://www.chathamhouse.org>
- Chazdon, R. L. (2008). Beyond deforestation: restoring forests and ecosystem services on degraded lands. *Science*, 320(5882), 1458-1460.
- Chazdon, R. L. (2014). *Second growth: The promise of tropical forest regeneration in an age of deforestation*. University of Chicago Press.
- Chica-Olmo, M., Abarca-Hernández, F., & Tolosana-Delgado, R. (2013). Land cover change analysis of a Mediterranean area in Spain using different sources of data: Multi-seasonal Landsat images, land surface temperature, digital terrain models and texture. *International Journal of Applied Earth Observation and Geoinformation*, 20, 37-49. <https://doi.org/10.1016/j.jag.2011.12.002>
- Congalton, R. G., & Green, K. (2019). *Assessing the Accuracy of Remotely Sensed Data: Principles and Practices* (3rd ed.). CRC Press.
- DeFries, R. S., Foley, J. A., & Asner, G. P. (2004). Land-use choices: Balancing human needs and ecosystem function. *Frontiers in Ecology and the Environment*, 2(5), 249-257.
- Demattê, J. A. M., Fongaro, C. T., Rizzo, R., & Safanelli, J. L. (2018). Geospatial Soil Sensing System (GEOS3): A powerful data mining procedure to retrieve soil spectral reflectance from satellite images. *Remote Sensing of Environment*, 212, 161-175. <https://doi.org/10.1016/j.rse.2018.04.047>
- Dethier, E.N., Silman, M., Leiva, J.D. et al. A global rise in alluvial mining increases sediment load in tropical rivers. *Nature* 620, 787-793 (2023). <https://doi.org/10.1038/s41586-023-06309-9>.
- Donkor, A., Nartey, V., Bonzongo, J. C., & Adotey, D. (2009). Artisanal mining of gold with mercury in Ghana. *West African Journal of Applied Ecology*, 9. <https://doi.org/10.4314/wajae.v9i1.45666>
- Duarte, F., Álvarez, M., & Gómez, J. (2017), quienes exploraron la clasificación de imágenes para análisis de la cobertura del suelo.
- Espejo, J. C., Messinger, M., Román-Dañobeytia, F., Ascorra, C., Fernandez, L. E., & Silman, M. R. (2018). Deforestation and forest degradation due to gold mining in the Peruvian Amazon: A 34-Year Perspective. *Remote Sensing*, 10(12), 1903. <https://doi.org/10.3390/rs10121903>
- Esri. (2023). How Accuracy Assessment works. ArcGIS Pro Documentation. <https://pro.arcgis.com/en/pro-app/latest/tool-reference/spatial-analyst/how-accuracy-assessment-works.htm>.
- Feeley, K. J., Davies, S. J., Perez, R., Hubbell, S. P., & Foster, R. B. (2011). Directional changes in the species composition of a tropical forest. *Ecology*, 92(4), 871-882.
- Fernández-Manso, A., Quintano, C., & Roberts, D. (2012). Evaluation of multiple endmember spectral mixture analysis (MESMA) for surface coal mining affected area mapping. *Remote Sensing of Environment*, 127, 181-193. <https://doi.org/10.1016/j.rse.2012.08.028>
- Franco, R. (2017). *Composiciones LANDSAT en ArcGis: Guía básica*. Bogotá, Colombia. 45p. Disponible en <http://wp.me/p2IwQU-1bh>
- Foody, G. M. (2002). Status of land cover classification accuracy assessment. *Remote Sensing of Environment*, 80(1), 185-201.
- Gastauer, M., Souza Filho, P. W. M., Ramos, S. J., Caldeira, C. F., Silva, J. R., Siqueira, J. O., & Furtini Neto, A. E. (2019). Mine land rehabilitation in Brazil: Goals and techniques in the context of legal requirements. *Am-bio*, 48(1), 74-88.
- Gerson, J. R., Szponar, N., Zambrano, A. A., et al. (2022). Amazon forests capture high levels of atmospheric mercury pollution from artisanal gold mining. *Nature Communications*, 13(1), 27997. <https://doi.org/10.1038/s41467-022-27997-3>
- Gillanders, S. N., Coops, N. C., Wulder, M. A., & Goodwin, N. R. (2008). Application of Landsat satellite imagery to monitor land-cover changes at the Athabasca Oil Sands, Alberta, Canada. *Canadian Geographer*. <https://doi.org/10.1111/j.1541-0064.2008.00225.x>
- Gistec. (2012). Comparison of NDVI and SAVI for vegetation detection. Retrieved from www.gistec.com
- González, M. (2015). Análisis espectral de sólidos suspendidos en aguas continentales con presencia de actividades mineras: caso de estudio Río Sipí, Pacífico Colombiano. *Universidad Militar Nueva Granada*, 14. <http://hdl.handle.net/10654/13462>
- Gorelick, N., Hancher, M., Dixon, M., Ilyushchenko, S., Thau, D., & Moore, R. (2017). Google Earth Engine: Planetary-scale geospatial analysis for everyone. *Remote Sensing of Environment*. <https://doi.org/10.1016/j.rse.2017.06.031>
- Hartigan, A., & Wong, M. A. (1979). A K-Means Clustering Algorithm. *Journal of the Royal Statistical Society*.
- He, D., Le, B. T., Xiao, D., Mao, Y., Shan, F., & Ha, T. T. L. (2019). Coal mine area monitoring method by machine learning and multispectral remote sensing images. *Infrared Physics and Technology*, 103, 1350-14495. <https://doi.org/10.1016/j.infrared.2019.103070>
- Helmi, S., & Banaei-Kashani, F. (2016). Mining frequent episodes from multivariate spatiotemporal event sequences. *Proceedings of the 7th ACM SIGSPATIAL International Workshop on GeoStreaming, IWGS 2016*. <https://doi.org/10.1145/3003421.3003428>
- Hengkai, L., Feng, X., & Qin, L. (2020). Remote sensing monitoring of land damage and restoration in rare earth mining areas in 6 counties in southern Jiangxi based on multisource sequential images. *Journal of Environmental Management*, 267, 1-9. <https://doi.org/10.1016/j.jenvman.2020.110653>
- Huang, D., & Liu, Q. (2013). Remote sensing monitoring and effect evaluation on ecological restoration of heidaigou coal mining area. *International Conference on Remote Sensing, Environment and Transportation Engineering, RSETE 2013*, 160-163. <https://doi.org/10.2991/rsete.2013.40>
- Huete, A. R. (1988). A soil-adjusted vegetation index (SAVI). *Remote Sensing of Environment*. [https://doi.org/10.1016/0034-4257\(88\)90106-X](https://doi.org/10.1016/0034-4257(88)90106-X)
- Ibrahim, E., Lema, L., Barnabé, P., Lacroix, P., & Pirard, E. (2020). Small-scale surface mining of gold placers: Detection, mapping, and temporal analysis through the use of free satellite imagery. *International Journal*

- of *Applied Earth Observation and Geoinformation*, 93(July), 102194. <https://doi.org/10.1016/j.jag.2020.102194>
- Karakacan Kuzucu, A., & Bektas Balcik, F. (2017). Testing the potential of vegetation indices for land use/cover classification using high resolution data. *ISPRS Annals of the Photogrammetry, Remote Sensing and Spatial Information Sciences*, 4, 279–283. <https://doi.org/10.5194/isprs-annals-IV-4-W4-279-2017>
- Karan, S. K., Samadder, S. R., & Maiti, S. K. (2016). Assessment of the capability of remote sensing and GIS techniques for monitoring reclamation success in coal mine degraded lands. *Journal of Environmental Management*, 182, 272–283. <https://doi.org/10.1016/j.jenvman.2016.07.070>
- Landis, J. R., & Koch, G. G. (1977). The Measurement of Observer Agreement for Categorical Data. *Biometrics*. <https://doi.org/10.2307/2529310>
- Lei, S., Ren, L., & Bian, Z. (2016). Time-space characterization of vegetation in a semiarid mining area using empirical orthogonal function decomposition of MODIS NDVI time series. *Environmental Earth Sciences*, 75(6), 1–11. <https://doi.org/10.1007/s12665-015-5122-z>
- Li, H., Lei, J., & Wu, J. (2017). Evolution analysis of vegetation cover under the disturbance of rare earth mining: A case in Lingbei mining area. *Journal of Applied Science and Engineering*, 20(3), 393–400. <https://doi.org/10.6180/jase.2017.20.3.14>
- Li, J., Liang, J., Wu, Y., Yin, S., Yang, Z., & Hu, Z. (2021). Quantitative evaluation of ecological cumulative effect in mining area using a pixel-based time series model of ecosystem service value. *Ecological Indicators*, 120. <https://doi.org/10.1016/j.ecolind.2020.106873>
- Li, J., Yan, X., Cao, Z., Yang, Z., Liang, J., Ma, T., & Liu, Q. (2020). Identification of successional trajectory over 30 Years and evaluation of reclamation effect in coal waste dumps of surface coal mine. *Journal of Cleaner Production*, 269. <https://doi.org/10.1016/j.jclepro.2020.122161>
- Lillesand, T., Kiefer, R. W., & Chipman, J. (2015). *Remote sensing and image interpretation* (7th ed.). John Wiley & Sons.
- Lu, D., Mausel, P., Brondizio, E., & Moran, E. (2004). Change detection techniques. *International Journal of Remote Sensing*, 25(12), 2365–2401.
- LU, X., HU, Z. q., LIU, W. jie, & HUANG, X. yan. (2007). Vegetation Growth Monitoring Under Coal Exploitation Stress by Remote Sensing in the Bulianta Coal Mining Area. *Journal of China University of Mining and Technology*, 17(4), 479–483. [https://doi.org/10.1016/S1006-1266\(07\)60129-1](https://doi.org/10.1016/S1006-1266(07)60129-1)
- Decreto 356 de 2018, 6 (2018). Recuperado de <https://www.funcionpublica.gov.co/eva/gestornormativo/norma.php?i=85440>
- Esri. (2020). ArcGIS Web AppBuilder (Version 2.15) [Computer software]. <https://www.esri.com/en-us/arcgis/products/web-appbuilder/overview>.
- McFeeters, S. K. (1996). The use of the Normalized Difference Water Index (NDWI) in the delineation of open water features. *International Journal of Remote Sensing*. <https://doi.org/10.1080/01431169608948714>
- McKenna, P. B., Lechner, A. M., Phinn, S., & Erskine, P. D. (2020). Remote sensing of mine site rehabilitation for ecological outcomes: A global systematic review. In *Remote Sensing*. <https://doi.org/10.3390/rs12213535>
- MDPI. (2023). *Assessing ecological restoration in arid mining regions: A progressive evaluation system*. Retrieved from <https://www.mdpi.com>
- Moore, I. D., Grayson, R. B., & Ladson, A. R. (1991). Digital terrain modelling: A review of hydrological, geomorphological, and biological applications.
- Olofsson, P., Foody, G. M., Herold, M., Stehman, S. V., Woodcock, C. E., & Wulder, M. A. (2014). Good practices for estimating area and assessing accuracy of land change. *Remote Sensing of Environment*, 148, 42–57.
- Pérez-Rincón, M. . (2014). Conflictos ambientales en Colombia: inventario, caracterización y análisis. In *Minería en Colombia: control público, memoria y justicia socio-ecológica, movimientos sociales y posconflicto*.
- Pérez Umaña, M. (2018). *Análisis multitemporal de la zona de explotación minera cielo abierto en el municipio de Duitama a partir de imágenes Landsat 7 y Sentinel 2A*. Universidad Militar Nueva Granada. <http://repository.unimilitar.edu.co/handle/10654/17633>
- Petropoulos, G. P., & Partsinevelos, P. (2012). Change detection of surface mining activity and reclamation based on a machine learning approach of multi-temporal Landsat TM imagery. *Geocarto International*, 28(4), 323–342. <https://doi.org/10.1080/10106049.2012.706648>
- Pueblo, D. del. (2015). *La Minería sin control, un enfoque desde la vulneración de los Derechos Humanos*. <https://www.defensoria.gov.co>
- Quejada Palacios, J. L. (2019). *Afectaciones por minería en la subzona hidrográfica del Río Quito, mediante la interpretación de imágenes satelitales*. Universidad de Manizales.
- Raval, S., & Shamsoddini, A. (2014). A monitoring framework for land use around kaolin mining areas through Landsat TM images. *Earth Sci Inform*. <https://doi.org/10.1007/s12145-014-0169-z>
- Remote Sensing: An Overview. Eart Data: Open Access for Open Science. NASA, 2022. Disponible en: <https://earthdata.nasa.gov/learn/backgrounders/remote-sensing>
- Richards, J. A. (2013). *Remote sensing digital image analysis: An introduction* (5th ed.). Springer.
- Rodríguez-Luna, S. (2012). *Localización de áreas de potencial explotación minera que no afectan la dinámica ambiental y territorial del municipio de Marmatón, utilizando Sistemas de Información Geográfica*. 67. <http://ridum.umanizales.edu.co:8080/xmlui/bitstream/handle/6789/999/SIG MINERIA ORDENAMIENTO TERRITORIAL Y AMBIENTAL.pdf?sequence=1>
- Rodríguez, I. C. C. (2018). *Evaluación de daños ambientales por minería a cielo abierto en un lecho fluvial en Colombia, usando imágenes multiespectrales*. Universidad de Manizales.
- Rodríguez, P. A. (2019). Evaluación de daños ambientales por explotación de oro de aluvión en los Humedales de Ayapel. Repositorio Institucional Universidad de Manizales. Disponible en: <https://ridum.umanizales.edu.co/xmlui/handle/20.500.12746/6255>.
- Saini, V., Ravi, G., & Manoj, A. (2019). Environmental Monitoring in the Jharia Coalfield, India. In *Coal and Peat Fires: A Global Perspective* (pp. 359–385). <https://doi.org/10.1016/b978-0-12-849885-9.00017-2>
- Salazar, A., Sanchez, A., Villegas, J. C., Salazar, J. F., Ruiz Carrascal, D., Sith, S., Restrepo, J. D., Poveda, G., Feeley, K. J., Mercado, L. M., Arias, P. A., Sierra, C. A., Uribe, M. del R., Rendón, A. M., Pérez, J. C., Murray Tortarolo, G., Mercado-Bettin, D., Posada, J. A., Zhuang, Q., & Dukes, J. S. (2018). The ecology of peace: preparing Colombia for new political and planetary climates. *Frontiers in Ecology and the Environment*, 16(9), 525–531. <https://doi.org/10.1002/fee.1950>
- Sonter, L. J., Herrera, D., Barrett, D. J., Galford, G. L., Moran, C. J., & Soares-Filho, B. S. (2017). Mining drives extensive deforestation in the Brazilian Amazon. *Nature Communications*, 8(1), 1013.
- Suarez Prada, H. S. (2019). *Protocolo de procesamiento de imágenes satelitales para el entrenamiento y prueba de una red neuronal de predicción de daño ecológico por extracción ilegal de minerales dentro del marco de celebración de los 100 años de la Fuerza Aérea Colombiana*. Universidad Distrital Francisco José de Caldas.
- Oficina de las Naciones Unidas contra la Droga y el Delito-UNODC (2016). *Colombia, Explotación de oro de aluvión. Evidencias a partir de percepción remota*, 2016. https://www.unodc.org/documents/colombia/2016/junio/Explotacion_de_Oro_de_Aluvion.pdf
- Oficina de las Naciones Unidas contra la Droga y el Delito-UNODC (2019). *Colombia, Explotación de oro de aluvión. Evidencias a partir de percepción remota*, 2018.
- Oficina de las Naciones Unidas contra la Droga y el Delito-UNODC (2021). *Explotación de oro de aluvión: Evidencias a partir de percepción remota* 2020.

- Qi, J., Chehbouni, A., Huete, A. R., Kerr, Y. H., & Sorooshian, S. (1994). A modified soil adjusted vegetation index (MSAVI). *Remote Sensing of Environment*, 48(2), 119–126.
- Talukdar, S., Singha, P., Mahato, S., Shahfahad, Pal, S., Liou, Y.-A., & Rahman, A. (2020). Land-Use Land-Cover Classification by Machine Learning Classifiers for Satellite Observations—A Review. *Remote Sensing*, 12(7), 1135. <https://doi.org/10.3390/rs12071135>.
- Uribe Ospina, D. (2019). *Estimación de la contaminación causada por la minería en cuerpos de agua del Bajo Cauca a través de imágenes satelitales*. Universidad EIA.
- U.S. Geological Survey. (n.d.). *Landsat soil adjusted vegetation index (SAVI)*. Retrieved January 16, 2025, from <https://www.usgs.gov/landsat-missions/landsat-soil-adjusted-vegetation-index>
- Wang, J., Yang, R., & Feng, Y. (2017). Spatial variability of reconstructed soil properties and the optimization of sampling number for reclaimed land monitoring in an opencast coal mine. *Arabian Journal of Geosciences*. <https://doi.org/10.1007/s12517-017-2836-0>
- Wang, X., Tan, K., Xu, K., Chen, Y., & Ding, J. (2019). Quantitative evaluation of the eco-environment in a coalfield based on multi-temporal remote sensing imagery: A case study of Yuxian, China. *International Journal of Environmental Research and Public Health*, 16(3). <https://doi.org/10.3390/ijerph16030511>
- What is remote sensing and what is it used for? | U.S. Geological Survey. Tomado de: <https://www.usgs.gov/faqs/what-remote-sensing-and-what-it-used>
- Wu, X., & Zhang, X. (2019). An efficient pixel clustering-based method for mining spatial sequential patterns from serial remote sensing images. *Computers and Geosciences*. <https://doi.org/10.1016/j.cageo.2019.01.005>
- Xu, J., Zhao, H., Yin, P., Jia, D., & Li, G. (2018). Remote sensing classification method of vegetation dynamics based on time series Landsat image : a case of opencast mining area in China. *EURASIP Journal on Image and Video Processing*, 113.
- Zaki, M. J. (2001). SPADE: An efficient algorithm for mining frequent sequences. *Machine learning*, 42, 31–60.
- Zhu, D., & Chen, T. (2020). Monitoring the effects of open-pit mining on the eco-environment using a moving window-based remote sensing ecological index. *Environmental Science and Pollution Research*. <https://doi.org/https://doi.org/10.1007/s11356-020-08054-2>.
- Zhu, Z., & Woodcock, C. E. (2014). Continuous monitoring of forest disturbance using all available Landsat imagery. *Remote Sensing of Environment*, 144, 163–175. <https://doi.org/10.1016/j.rse.2014.01.011>